Applied Catalysis B: Environment and Energy 351 (2024) 123973

Contents lists available at ScienceDirect

Applied Catalysis B: Environment and Energy

journal homepage: www.elsevier.com/locate/apcatb

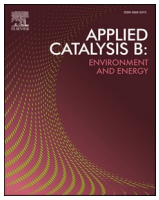

Designing a self-breathing electrode modulated by spatial hydrophobic microenvironments with stabilized H_2O_2 generation for wastewater treatment

Yingshi Zhu [a,b], Jianqiu Zhu [b], Huabin ShenTu [c], Genman Lin [b], Jun Wei [c], Yanfei Wei [b], Lecheng Lei [a,d], Yuru Li [b], Tao Yu [b], Zhongjian Li [a,d], Yang Hou [a,d], Bin Yang [a,d,*]

[a] Key Laboratory of Biomass Chemical Engineering of Ministry of Education, College of Chemical and Biological Engineering, Zhejiang University, Hangzhou 310058, China
[b] Office of Scitech Research, Zhejiang Environment Technology Co., Ltd., Hangzhou 311100, China
[c] Power China Huadong Engineering Co., Ltd., Hangzhou 311112, China
[d] Institute of Zhejiang University-Quzhou, No. 99 Zheda Road, Quzhou 324000, China

ARTICLE INFO

Keywords:
Rod graphite
Self-breathing
H_2O_2 accumulation
Oxygen transfer
Wastewater treatment

ABSTRACT

A novel self-breathing air-diffusion rod graphite electrode (ADE-RG) engineered with spatial hydrophobic microenvironments was developed to enhance H_2O_2 production without external air aeration. The microenvironments, created through thermal shaking-induced turbulence and centrifugal effect, significantly improved the air-diffusion capability. This innovation led to the increase in H_2O_2 generation (3.36 times higher than that in the unmodified system) due to a locally enhanced electric field, increased oxygen transfer rate, and improved selectivity for two-electron transfer process. Furthermore, incorporating polyepoxysuccinic acid into the electrolyte not only prevents electrode scaling but also minimizes H_2O_2 decomposition, culminating in the H_2O_2 concentration of 50.64 ± 2.92 mg L^{-1} cm^{-2}. Notably, the system performed prominently in treating industrial rifampicin wastewater, achieving a degradation efficiency of 95.29 ± 0.47%, even under high-loading conditions (initial COD was 22,898.50 ± 405.17 mg L^{-1}). These results indicate the significant potential of the self-breathing ADE-RG system in broad-scale wastewater treatment applications.

1. Introduction

H_2O_2 is a widely utilized industrial chemical, essential in various advanced oxidation processes (AOPs) such as Fenton, O_3/H_2O_2, light/H_2O_2 and peroxymonosulfate (PMS)/H_2O_2, etc. [1–4]. However, conventional H_2O_2 production through the anthraquinone process is complex and unfriendly, generating significant waste [5]. Moreover, due to its instability and H_2O_2 is unstable and storage challenges, in-situ H_2O_2 synthesis become crucial for industrial applications. As indicated in Eq. 1, electrochemical synthesis of H_2O_2 presents a more flexible and safer alternative compared to traditional methods in wastewater treatment [6], focusing on the two electron transfer oxygen reduction reaction ($2e^-$-ORR) mechanism [7].

$$O_2 + 2H^+ + 2e^- \rightarrow H_2O_2 \quad (1)$$

Carbon-based materials, recognized for their non-toxicity and cost-effectiveness, are often employed in $2e^-$-ORR electrodes [8–10]. Carbon felts, characterized by micron-scale diameter and porous three-dimensional network structure, provide excellent electrical conductivity. The porous network structure not only offers active sites for catalyst loading but also facilitates catalyst dispersion [11], thereby enhancing $2e^-$-ORR via improving electron transfer and the H^+ utilization [12]. Furthermore, doping carbon materials with heteroatoms (N, O, F, B, S etc.) can redistribute electron density, thereby augmenting their intrinsic catalytic activity [13]. Among them, oxygen doping has received extensive attention for its simplicity and environmental friendliness [14].

The efficacy of the $2e^-$-ORR is limited by oxygen mass transfer rate, constrained by the low solubility of oxygen in water (8.1–8.5 mg L^{-1} at 25℃) and modest diffusion coefficient (1.96–2.56 × 10^{-9} m^2 s^{-1} at

* Corresponding author at: Key Laboratory of Biomass Chemical Engineering of Ministry of Education, College of Chemical and Biological Engineering, Zhejiang University, Hangzhou 310058, China.
E-mail address: keyangb@zju.edu.cn (B. Yang).

https://doi.org/10.1016/j.apcatb.2024.123973
Received 30 January 2024; Received in revised form 11 March 2024; Accepted 16 March 2024
Available online 19 March 2024

25℃) [15]. To address this, extensive research has been conducted on gas diffusion electrodes (GDEs), particularly focusing on hydrophobic surface modification to improve the oxygen transfer [16–18]. However, the traditional GDEs primarily utilize dissolved oxygen in water and not from air, due to a lack of internal gas transfer channels, thereby resulting in low oxygen utilization (<1%) [19,20]. Designing an electrode with spatial hydrophobic microenvironments can overcome this limitation by providing gas transfer channels within the electrode, thus establishing efficient gas-liquid-solid three-phase interfaces and significantly boosting oxygen mass transfer.

Maintaining a high concentration of H_2O_2 in electrochemical system poses a challenge due to its rapid decomposition after reaching a certain level [21]. Ensuring H_2O_2 stability is therefore a critical aspect to address. Previous research has indicated that additives like polyacrylic acid can stabilize H_2O_2 and reduce its decomposition in the system [22]. Another significant issue is scale formation on the electrode surface, commonly caused by the presence of ions like Ca^{2+} and Mg^{2+} in wastewater and high alkalinity near the cathode. This scale formation can obstruct active sites on the cathode, leading to a marked decrease in H_2O_2 generation efficiency [23]. The use of scale inhibitors has been a common approach to prevent electrode precipitation [24]. It is a grand challenge of underscoring the need to identify suitable additives in the electrolyte that can both stabilize H_2O_2 and inhibit scale formation.

In our study, we introduce rod graphite (RG) as a novel conductive agent for H_2O_2 generation, leveraging its unique structure to enhance the local electric field and thereby drive efficient electron transfer. We have employed turbulence and centrifugal force in the electrode fabrication process strategically integrated into the hydrophobic binder polytetrafluoroethylene (PTFE) to create internal channels, forming a hydrophobic microenvironment conducive to significantly improve oxygen mass transfer during $2e^-$-ORR. Additionally, RG was modified by oxygen atom during high-temperature calcination to enhance catalytic activity and selectivity for the $2e^-$-ORR. A key breakthrough in our research is the successful integration of polyepoxysuccinic acid (PESA) into the electrolyte, achieving dual objectives: stabilization of H_2O_2 and inhibition of scale formation on the electrode. Ultimately, this led to the development of an electro-Fenton system equipped with a self-breathing air-diffusion rod graphite electrode (ADE-RG), demonstrating its effectiveness in in-situ H_2O_2 synthesis and application for industrial pharmaceutical wastewater treatment.

2. Materials and methods

2.1. Fabrication of ADEs

Materials and reagents used were detailed in Supplementary Text S1. Air-diffusion electrodes (ADEs) were prepared through a systematic process involving mixing and calcination in a shaking bed, as shown in Fig. S1. Initially, RG or or normal flake graphite (NFG) was uniformly dispersed in ethanol, facilitated by ultrasonication for a duration of 5 min. This was followed by the addition of a 300 μL aliquot of 10 wt% PTFE dispersion and further ultrasonication, coupled with emulsion breaking for 10 min. Integration of carbon felt was executed meticulously to ensure uniform mixing. The shaker temperature was regulated at 50℃, and the agitation speed set at 150 rpm until the ethanol evaporated completely. The resultant mixture was then transferred to a tube furnace and subjected to a temperature of 300℃ for 40 min (heating rate of 5 ℃ min^{-1}), culminating in the formation of ADE-RG or ADE-NFG.

For the preparation of O-doped ADE-RG, RG was initially subjected to calcination treatment in a tube furnace at 400–600℃ for 30 min (heating rate of 10 ℃ min^{-1}) in the absence of a protective gas to introduce oxygen atoms (labeled O400, O500, O600). The ensuring steps were a mirror to the initial fabrication process, resulting in the creation of ADE-RG-O400, ADE-RG-O500 and ADE-RG-O600, respectively.

2.2. Electrochemical experiments

A 100 mL 0.05 M Na_2SO_4 was employed as the electrolyte for H_2O_2 accumulation. A titanium-based metal oxide coated electrode (SnO_2 + SbO_2) served as the anode, while the fabricated ADEs were utilized as cathodes (2 cm × 2 cm). The electrode distance was 2 cm, and a magnetic stirring was operated at 500 rpm to ensure solution homogeneity. The configuration of the electrochemical setup is illustrated in Fig. S2. Levels of H_2O_2 were quantified every 10 minutes by sampling 100 μL of the electrolyte. O-doped ADE-RG was employed as the cathode to enhance the H_2O_2 selectivity. The generated H_2O_2 was stabilized by adding 10 mg L^{-1} of additives including sodium polyphosphate (PP), sodium polyacrylate (PAAS) and PESA. Furthermore, the stabilization against high concentration of H_2O_2 with additives was evaluated by introducing 200 mg L^{-1} H_2O_2 into the electrolytic cell prior to the reaction. Subsequently, Fe^{2+} was introduced to establish an electro-Fenton system for the treatment of pharmaceutical wastewater. Detailed methodologies for characterization, analysis and simulation were provided in Supplementary Text S2.

3. Results and discussion

3.1. Electrode preparation with hydrophobic microenvironments

In the design of the ADE-RG, as illustrated in Fig. 1a, RG was strategically integrated into the hydrophobic binder PTFE, forming a hydrophobic microenvironment conducive to effective oxygen transfer, essential for H_2O_2 production. The SEM image of the selected RG was shown in Fig. S3. Moreover, the turbulence and centrifugal effect generated during the electrode fabrication in the shaking bed contributed to the formation of spatial hydrophobic microenvironments, as evidenced by the cross-section in Fig. 1b. These microenvironments are instrumental in facilitating oxygen transfer for H_2O_2 production. Furthermore, Fig. S4 illustrates that without shaking or with the low shaking speed, the spatial hydrophobic microenvironment could not be formed inside the carbon felt due to the lack of turbulence and centrifugal effect and was only formed at the bottom of the carbon felt. The efficacy of spatial hydrophobic microenvironments is quantitatively demonstrated in Fig. 1c and Fig. S5. Initially, the raw carbon felt (SEM image in Fig. S6) managed to accumulate only 13.12 ± 0.63 mg L^{-1} cm^{-2} H_2O_2 after 60 min of operation. However, when modified with NFG (SEM image in Fig. S7) and RG, the H_2O_2 accumulation surged to 33.18 ± 0.97 mg L^{-1} cm^{-2} and 38.55 ± 0.36 mg L^{-1} cm^{-2}, respectively, achieving 152.90% and 193.83% increments compared to that before modification. This notable increase can be attributed to the transition from a hydrophilic to a hydrophobic surface, as evidenced by the increase in contact angle with water from 88.1° for the raw carbon felt to 129.4° and 128.1° for NFG and RG, respectively. This transformation enhances the adsorption of gaseous oxygen from the air to the electrode interface [25]. In addition, Fig. S5 shows that the electrode capacity for H_2O_2 production was much lower than that of ADE-RG without the formation of spatial hydrophobic microenvironments.

Despite the enhancements observed with both NFG and RG modifications, ADE-RG outperformed ADE-NFG in terms of H_2O_2 accumulation. Considering the similar electrical resistivity of NFG (13 μΩ·m) and RG (14 μΩ·m), XRD experiments were conducted to investigate the crystal structure of NFG and RG which may affect the H_2O_2 generation. As shown in Fig. 1d, both NFG and RG displayed characteristic diffraction peaks at 2θ of 26.6° and 44.6°, correlating with the (0 0 2) and (1 0 1) planes of graphite (PDF#89–8487). This suggests that the distinct morphologies of NFG and RG might affect the H_2O_2 generation. To elucidate this, multi-physics field simulations were conducted using COMSOL. Fig. 1e and Fig. 1 f reveal that RG exhibits a stronger electric field strength at its vertices compared to NFG, potentially offering a continuous pathway for electron transfer and thereby facilitating a rapid reaction through localized strong electric field [26]. Moreover, Fig. 1 g,

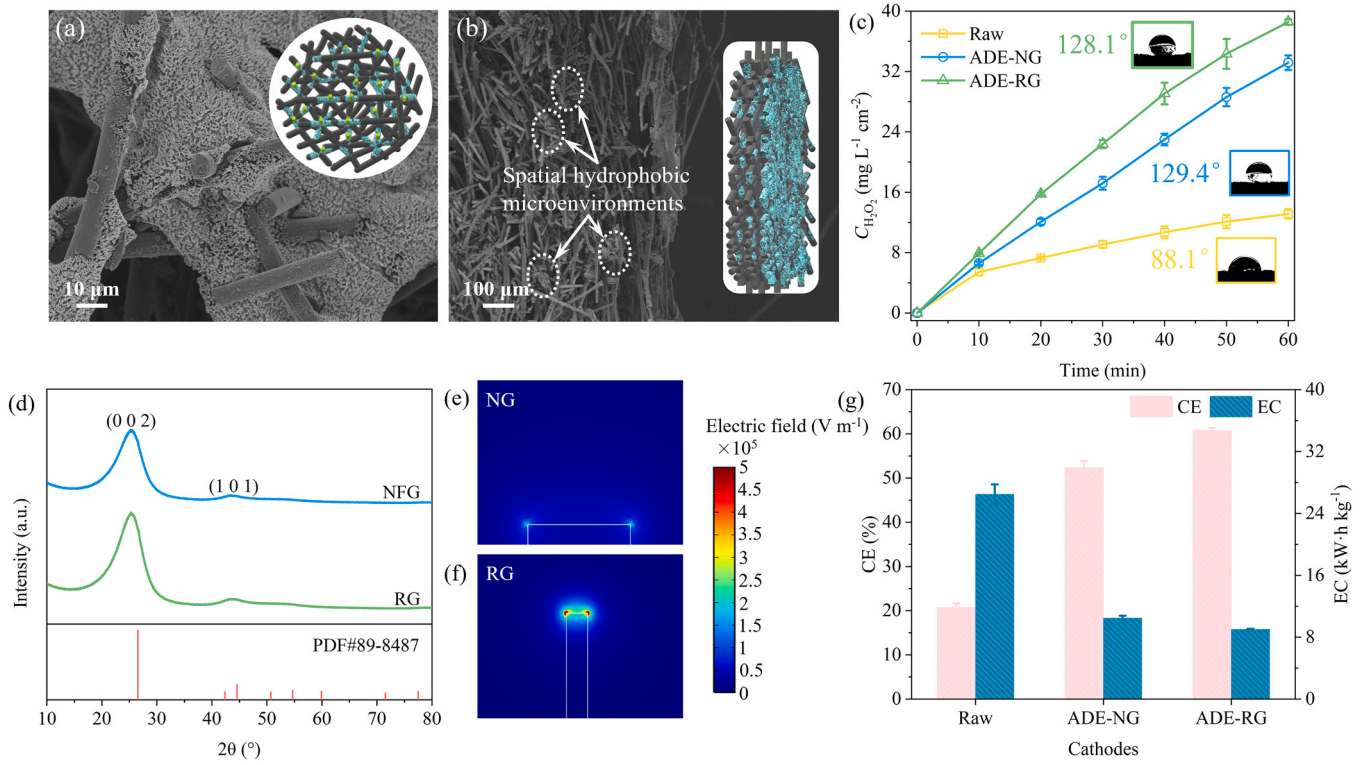

Fig. 1. SEM (a) surface and (b) cross-section images of ADE-RG. (c) The H_2O_2 accumulation and contact angle of different cathodes. (d) XRD patterns of NFG and RG. The distribution of electric field with (e) NFG and (f) RG. (g) CE/EC of different cathodes. Conditions: neutral pH and current density = 10 mA cm^{-2}.

showcases a significant improvement current efficiency (CE, Eq. S1) when RG and NFG were used as the conductive agent, rising to the 60.77 ± 0.57% and 52.30 ± 1.53%, respectively, from the 20.68 ± 1.00% observed with the unmodified carbon felt. Additionally, the energy consumption (EC, Eq. S2) of the ADE-RG was notably reduced, standing at only 34% of that of the unmodified carbon felt. Figs. S8-S10 further

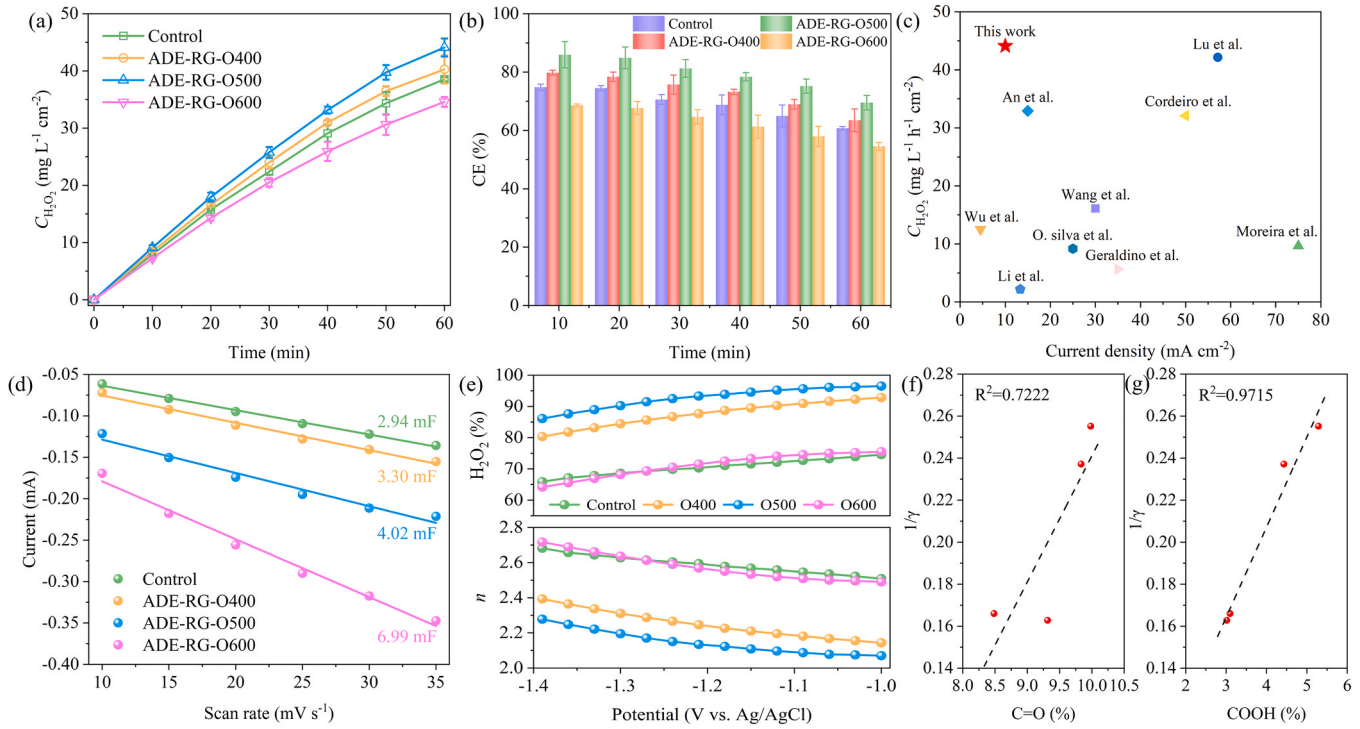

Fig. 2. (a) The H_2O_2 accumulation and (b) CE of different cathodes. (c) Comparison of $C_{H_2O_2}$ using ADE-RG-O500 with literature. (d) current-scan rates curves, (e) H_2O_2 selectivity and electron transfer number of different cathodes. 2e$^-$-ORR selectivity (1/γ) as a function of (f) C=O and (g) COOH. Conditions: neutral pH and current density = 10 mA cm^{-2}.

affirm that an optimal ratio of m_{PTFE}/m_{RG} and m_{RG} can provide an ideal hydrophobic microenvironment, bolstering the system's efficiency.

3.2. Boosting H_2O_2 generation by O-doped ADE-RG

The augmentation of the catalytic activity and selectivity for 2e⁻-ORR was pursued by doping RG with oxygen via high-temperature calcination. Fig. S11a shows that the oxygen content in the catalyst gradually increased with the increase of calcination temperature. In addition, the FTIR spectra in Fig. S11b illustrate that the C═O vibrational peaks in O500 increased significantly after oxygen doping, making ADE-RG-O500 electrode exhibited superior H_2O_2 accumulation and reaching an impressive capacity of 44.09 ± 1.58 mg L^{-1} cm^{-2}. Moreover, the amount of H_2O_2 accumulated by the ADE-RG-O600 electrode (34.59 ± 0.86 mg L^{-1} cm^{-2}) was lower than that of the control electrode (38.55 ± 0.36 mg L^{-1} cm^{-2}) for without oxygen doping. Fig. 2b illustrates that ADE-RG-O500 maintained the highest CE throughout the reaction, peaking at 85.96 ± 4.48% at 10 min and maintaining a robust value of 69.51 ± 2.49% at 60 min of reaction. This observation underscores the sustained catalytic ability of the electrode over time. To contextualize the significance of these results within the broader research landscape, a comparative study was conducted against existing literature (Fig. 2c), affirming that this study achieved the highest H_2O_2 accumulation even when the applied current density was not the highest [27–35].

Electrochemical double layer capacitance (EDLC) was calculated by performing cyclic voltammetry CV tests at different sweep speeds (Fig. S12), representing a metric to gauge the augmentation of electrochemically active sites [36]. Fig. 2d reveals that the increase of EDLC value for oxygen doping is indicative of enhanced charge transfer capabilities in the non-Faraday region between the electrode and the electrolyte. It's noteworthy that ADE-RG-O600, despite having the highest EDLC value of 6.99 mF, did not correspond to the highest H_2O_2 accumulation as shown in Fig. 2a. This discrepancy underscores the nature of ORR, where a balance between catalytic activity and two-electron transfer selectivity is paramount for optimal H_2O_2 generation. Further insights into the system were investigated through the rotating ring disk electrode (RRDE) test at 1600 rpm (Fig. S13). The data calculated by Eq. S3 reveals that O500 exhibited the highest H_2O_2 selectivity, aligning with the observed H_2O_2 accumulation trends (Fig. 2e). This selectivity, coupled with an electron transfer number of O500 closest to 2, confirms the effective execution of 2e⁻-ORR (Eq. S4). In contrast, O600 showed lower H_2O_2 selectivity despite its high ORR activity, and an electron transfer number close to 3, indicating simultaneous 4e⁻- ORR performance.

Doping oxygen forms different types of oxygen-containing functional groups such as C-OH, C═O, and COOH, but theoretical calculations have revealed that modifying C═O and COOH provides the active sites for 2e⁻-ORR [37]. XPS analysis was instrumental in identifying the functional groups (C═O and COOH) pivotal to H_2O_2 production (Fig. S14). The high-resolution XPS C1s spectra unveiled peaks at the binding energy of 288 eV and 291 eV corresponding to C═O and COOH, respectively [38]. Moreover, 1/γ which represents 2e⁻-ORR was calculated by Eq. 2 [39].

$$\frac{1}{\gamma} = \frac{2N I_{Ring}}{I_{Disk}} \tag{2}$$

The correlation between functional groups and 2e⁻-ORR performance is illustrated in Fig. 2 f and Fig. 2 g. The contents for C═O and COOH both exhibit positive correlation with 1/γ of an R^2 of 0.7222 and 0.9715, respectively, which underscores the critical role of these functional groups in the facilitation and optimization of H_2O_2 generation from 2e⁻-ORR. In addition, the different correlation between C═O and COOH with 1/γ is due to the large difference in catalytic activity for 2e⁻-ORR by the active sites induced by C═O at different positions of the carbon structure [40].

3.3. Optimization and comparison of ADE-RG for H_2O_2 generation

The effects of solution pH and the applied current density on H_2O_2 accumulation were investigated, establishing the pivotal operating conditions for the system. As illustrated in Fig. 3a, the ADE-RG-O500 demonstrated remarkable adaptability across a broad pH range of 3–9, with negligible variations in H_2O_2 accumulation. This finding underscores the versatility and robustness of the electrode design. Furthermore, a direct correlation was observed between applied current density and H_2O_2 accumulation, peaking at an impressive 59.74 ± 1.89 mg L^{-1} cm^{-2}. However, an inverse relationship was noted with current efficiency, diminishing as the applied current density decreased, where the CE was 74.45 ± 1.29% at 5 mA cm^{-2} and only 47.09 ± 1.49% was obtained when CE increased to 20 mA cm^{-2}. The critical balance between H_2O_2 production and energy efficiency should be considered. Consequently, an optimal current density of 10 mA cm^{-2} was selected, harmonizing the trade-off between CE and H_2O_2 production.

The electrode's performance was further investigated under different operational modes: fully immersed cathode (mode 1), self-breathing cathode (mode 2), and self-breathing cathode supplemented with additional aeration (mode 3), as depicted in Fig. 3b. The comparative analysis, illustrated in Figs. 3c and 3d, reveals a stark contrast in H_2O_2 accumulation across the modes. Mode 1 exhibited the lowest H_2O_2 accumulation (16.69 ± 0.77 mg L^{-1} cm^{-2}), attributable to the low dissolved oxygen concentration and constrained oxygen transfer in the electrolyte. Conversely, the mode 2 and mode 3 demonstrated significantly higher H_2O_2 accumulation, nearly triple that of mode 1, achieving 44.09 ± 1.58 mg L^{-1} cm^{-2} to 45.80 ± 0.83 mg L^{-1} cm^{-2}, respectively, which emphasized the efficacy of the self-breathing mechanism in enhancing oxygen transfer for ORR. Notably, the marginal difference between mode 2 and mode 3 suggests that the self-breathing cathode autonomously sources adequate oxygen for ORR, diminishing the necessity for external aeration devices. It revealed that while aeration enhances the oxygen supply to ADE-RG-O500 by providing a robust driving force, it does not proportionally increase H_2O_2 production. This discrepancy is attributed to the oxygen consumption limitations inherent in ORR. Remarkably, ADE-RG-O500 demonstrates adequate oxygen acquisition for H_2O_2 synthesis through self-breathing, hereby negating the necessity for auxiliary aeration apparatus. Furthermore, the effective oxygen diffusion coefficient (D_{eff}) can be calculated by Eq. 3 [41]:

$$n_{O_2} = D_{eff}\frac{\Delta C}{\Delta x} \tag{3}$$

where n_{O_2} is the flow rate of oxygen (mol m^{-2} s^{-1}), ΔC is the difference in concentration of through-plane (mol m^{-3}), Δx is the length of through-plane substrate (m).

Empirical data indicates that the D_{eff} values in air water are 2.00 × 10^{-5} m^2 s^{-1} (mode 3) and 2.10 × 10^{-9} m^2 s^{-1} (mode 1), respectively [42]. Under the presumption of 100% oxygen utilization efficiency, the effective mass transfer rate of oxygen was about 0.52 mM h^{-1}, based on H_2O_2 accumulation. The D_{eff} for self-breathing electrode (mode 2) is determined to be a minimum of 2.56 × 10^{-6} m^2 s^{-1}, approximately 13% of the D_{eff} in air and three orders of magnitude superior to that of dissolved oxygen in water (Fig. 3d). These findings underscore the efficacy of self-breathing ADE in facilitating gas-phase oxygen transportation, thereby improving the oxygen transfer process.

3.4. Stabilization of H_2O_2 and inhibition of scale formation on electrode

The stabilization of H_2O_2 in the electrochemical system represents a crucial facet of enhancing its practical application. As shown in Fig. 4a, the introduction of additives such as sodium polyphosphate (PP), sodium polyacrylate (PAAS) and polyepoxysuccinic acid (PESA) into the electrolyte was investigated for their stabilizing effect on H_2O_2. The

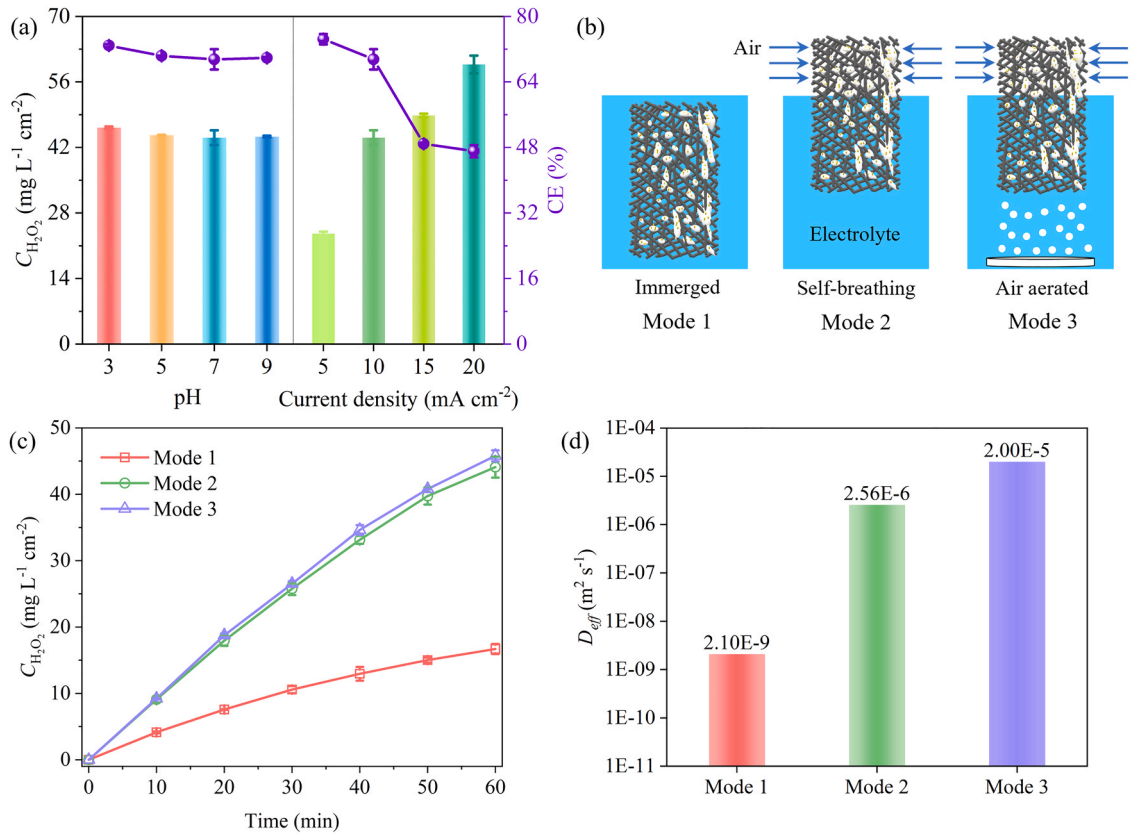

Fig. 3. (a) Effect of pH and current density on H_2O_2 accumulation. (b) Diagram of the three operating modes of ADE-RG-O500. (c) H_2O_2 accumulation and (d) D_{eff} of mode 1–3. Conditions: neutral pH and current density = 10 mA cm^{-2}.

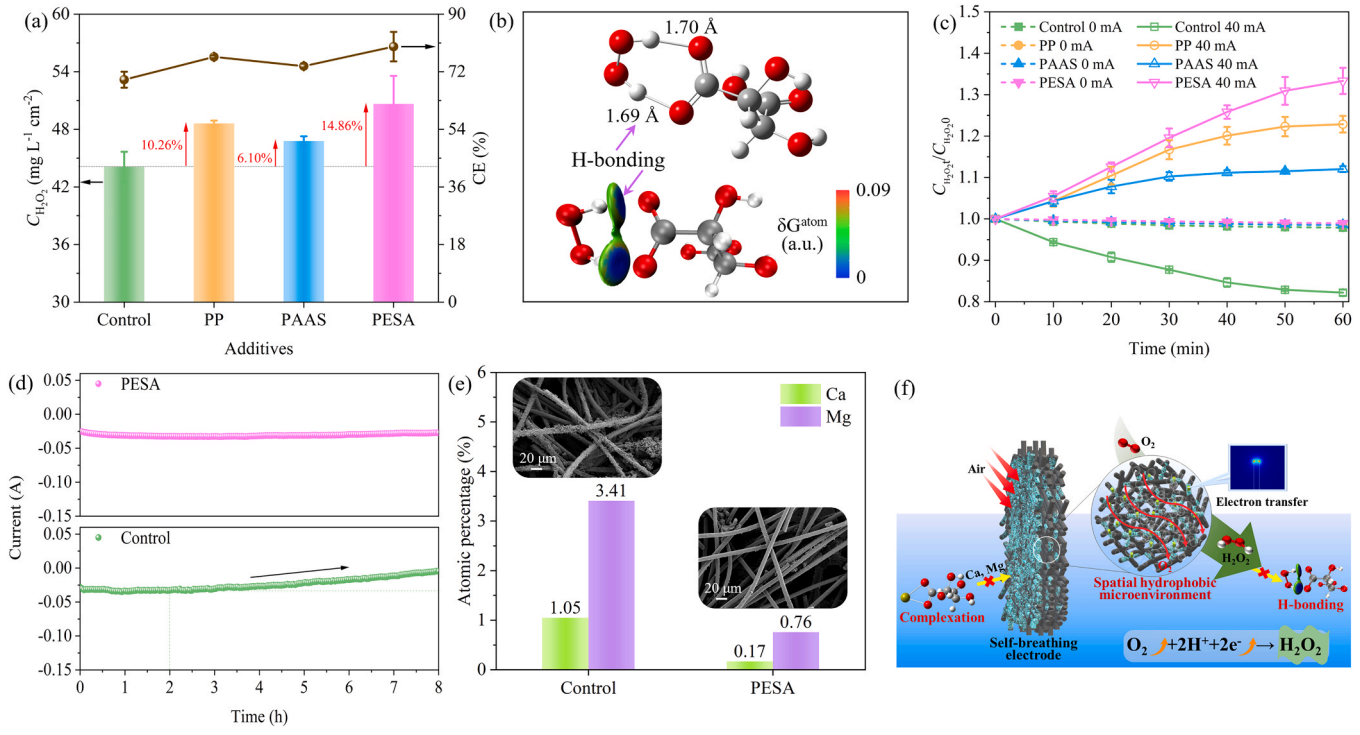

Fig. 4. (a) The H_2O_2 stabilization by adding different additives. (b) The optimized structure and *Sign*(λ_2)ρ colored isosurfaces of δg^{inter} = 0.01 a.u. of H_2O_2-PESA complex. (c) The H_2O_2 variations with initial concentration of 200 mg L^{-1}. (d) Inhibition of scale formation by adding PESA in 0.1 M $NaNO_3$ with 100 mg L^{-1} Ca^{2+}, 50 mg L^{-1} Mg^{2+} at a potential of −1.0 V *vs.* Ag/AgCl. (e) Atomic percentage of Ca/Mg and SEM images of cathode after 8 h reaction. (f) Scheme of this study.

study quantitatively demonstrates that H_2O_2 accumulation notably increased to 48.61 ± 0.31 mg L^{-1} cm^{-2}, 46.78 ± 0.49 mg L^{-1} cm^{-2} and 50.64 ± 2.92 mg L^{-1} cm^{-2} upon the introduction of respective additives. Correspondingly, the observed augmentations in H_2O_2 concentrations were 10.26%, 6.10% and 14.86%, respectively. Notably, the CE exhibited a significant enhancement, escalating from a pre-additive value of 69.51 ± 2.49% to a peak of 79.84 ± 4.61% subsequent to the incorporation of PESA. This phenomenon is elucidated through the lens of density functional theory which determines the interaction between PESA and H_2O_2. As represented in Fig. 4b, the carboxyl group's dual oxygen atoms in PESA engage in H-bonding with the two hydrogen atoms of H_2O_2, conferring stability to the H_2O_2 molecules. Furthermore, the interaction is visually depicted through the independent gradient model based on the Hirshfeld partition (IGHM) method, where the presence of H-bonding the between PESA and H_2O_2 is signified by the emergence of isosurfaces [43].

Fig. 4c illustrates the electrolysis process experienced a continual drop in the $C_{H_2O_2t}/C_{H_2O_20}$ ratio in the absence of additive, signifying that the decomposition of H_2O_2 exceeded the production. A comparative analysis of the stabilizing effects of PP, PAAS, and PESA on H_2O_2 was further conducted. Not only did PESA preserve the initial H_2O_2 concentration of 200 mg L^{-1}, but it also facilitated an increase in concentration under electrolysis, outperforming PP and PAAS. This clearly indicates that PESA significantly mitigates H_2O_2 decomposition through H-bonding, thereby enhancing its stability and concentration in the system, far more effectively than PP and PAAS.

Furthermore, the presence of Ca^{2+} and Mg^{2+} ions in natural water or wastewater, compounded by the interface's alkalinity of cathode due to proton consumption, prompts the scaling of metals ion [44], which is a critical factor during practical H_2O_2 production. To examine the scale inhibition, temporal current variation was analyzed (Fig. 4d). The control condition exhibited a marked current escalation after 2 hours of operation, indicative of the decrease in electrode performance due to the scaling at the cathode interface. Contrastingly, the system by the introduction of PESA maintained stable currents for up to 8 h, implying an impediment to scale formation. Fig. 4e and SEM images verify this and demonstrating a dramatic reduction in Ca and Mg deposition and a minimal atomic percentage post-PESA addition, where the atomic percentage dropped to less than one-fourth of that in the control. Moreover, thinner scale on the electrode for the addition of PESA was presented in Fig. 4e and Fig. S15, suggesting a potential for prolonged electrode lifespan. This effect is attributed to PESA's ability to chelate with Ca^{2+} and Mg^{2+} ions, preventing them from precipitating onto the electrode interface (Fig. S16). Rifampicin is an antibiotic classified as an essential drug by the World Health Organization but detected in the effluent of sewage treatment plants [45]. The effect of adding PESA on pollutant removal was investigated using rifampicin as the target pollutant. As shown in Fig. S17, the removal of rifampicin in the control system was 96.30 ± 2.25%, whereas 96.66 ± 2.31% of rifampicin was removed by the system with PESA, indicating that PESA would not interrupt the removal of contaminants from the system during stabilization of H_2O_2 and prevention of electrode scaling.

An integrative mechanism underlying the H_2O_2 production and stabilization in the system was proposed in Fig. 4 f. The process unfolds through a series of interrelated steps: (I) oxygen is systematically directed to the cathode's entire three-phase interface, facilitated by the inherent self-breathing attribute of the exposed cathode; (II) RG significantly amplifies local electric field, thereby enhancing electron transfer and reinforcing ORR; (III) subsequently, oxygen engaged at the cathodic three-phase interface is converted into H_2O_2 through a $2e^-$-ORR; (IV) the strategic introduction of PESA acts as a stabilizer for H_2O_2, effectively preventing its decomposition and boosting an increase in H_2O_2 accumulation; (V) in the presence of Ca^{2+} and Mg^{2+} ions, the additives demonstrate an inherent capacity to form complexes with these metal ions, thereby preventing from scale formation at the cathode interface and substantially enhancing the electrode's durability.

3.5. Application in pharmaceutical wastewater treatment

In a significant stride toward environmental remediation, the potential of the self-breathing and H_2O_2-stabilizating electrochemical system was rigorously evaluated for its efficacy in pharmaceutical wastewater treatment. An electro-Fenton system was developed, wherein the cathodically generated H_2O_2 interacts with Fe^{2+} to catalyze the formation of ·OH, crucial for the degradation pollutants [46]. The rifampicin pharmaceutical wastewater used in the experiment, sourced from a Zhejiang pharmaceutical factory, was characterized by a notably COD concentration of 22,898.50 ± 405.17 mg L^{-1} and a rifampicin concentration of 56.87 ± 2.06 mg L^{-1} (Table S1).

Fig. 5a elucidates the relationship between applied current density, initial pH, and Fe^{2+} dosage on the change in COD before and after the electro-Fenton system (ΔCOD). Notably, at a lower current density of 10 mA cm^{-2}, the system achieved a modest reduction of 6499.36 mg L^{-1} in COD, underscoring a dissociation between H_2O_2 production efficiency and ΔCOD removal. A subsequent increment in current density to 40 mA cm^{-2} failed to enhance the ΔCOD removal in contrast to 30 mA cm^{-2}, indicating the predominance of side reaction at elevated current density, including H_2/O_2 evolution and H_2O_2 decomposition [47]. Additionally, pH profoundly influences the speciation of iron ions with H_2O_2, which in turn affects the generation of ·OH radicals [48]. Consequently, an increase in pH was found to diminish the ΔCOD removal, attributable in part to the reduced oxidation potential of ·OH at higher pH levels [49]. Moreover, the ΔCOD removal initially increased with the addition of Fe^{2+} dosage within a certain range. However, excessive Fe^{2+} led to consumption of·OH ($k = 3.2 \times 10^8$ M^{-1} s^{-1}), ultimately resulting in a decline in COD removal [50]. Comparative analysis among the three anode electro-Fenton systems, as depicted in Fig. S18, revealed the highest COD efficiency of 60.21 ± 1.58% for the BDD anode electro-Fenton system was achieved. In contrast, the SnO_2 + SbO_2 and IrO_2 + TaO_2 anode systems exhibited identical COD removal of 32.10 ± 0.87%. Furthermore, the percentage of anodic oxidation and Fenton catalysis in the BDD system was examined. As shown in Fig. S19, anodic oxidation of BDD played a major role in COD removal with 69.72%, while Fenton catalysis accounted for 30.28%.

The electro-Fenton system demonstrated remarkable pollutant removal capabilities under optimal conditions. As depicted in Fig. 5b, a removal rate of COD of 60.21 ± 1.58% and an impressive removal of rifampicin of 95.29 ± 0.47% after 6 hours of electrolysis were achieved. The transformation of the wastewater from a dark color to a transparent light-yellow liquid over the treatment duration is evidence to the system's effectiveness (Fig. 5c). Additionally, approximate 20% removal rates of NH_4^+ and TN were simultaneously achieved, which is attributed to oxidation of Cl^- in the wastewater to HClO at the anode and subsequently reacts with NH_4^+ to form N_2 [51]. Fig. 5d elucidates the temporal dynamics of toxicity in rifampicin wastewater treated by the electro-Fenton system, utilizing *Vibrio fischeri* as a bio-indicator. Initially, the toxicity exhibited a pronounced increase, peaking at 85.77 ± 0.40%, attributed to the formation of aromatic/cyclic intermediates and active chlorine which possess higher toxicity than the parent contaminant [52,53]. However, with prolonged treatment duration, these toxic intermediates were effectively degraded, culminating in a substantial decrease in bio-inhibition to 13.57 ± 0.41%. This trend underscores the electro-Fenton system's capability to not only mitigate high COD and high antibiotic content in rifampicin wastewater but also significantly alleviate the bio-inhibition load on subsequent biological treatment processes.

4. Conclusion

In this research, we innovatively developed a novel self-breathing ADE-RG system, modulated by hydrophobic microenvironments, and established a H_2O_2-stabilization electrochemical system augmented with additives. RG exhibited local strong electric field strength at the

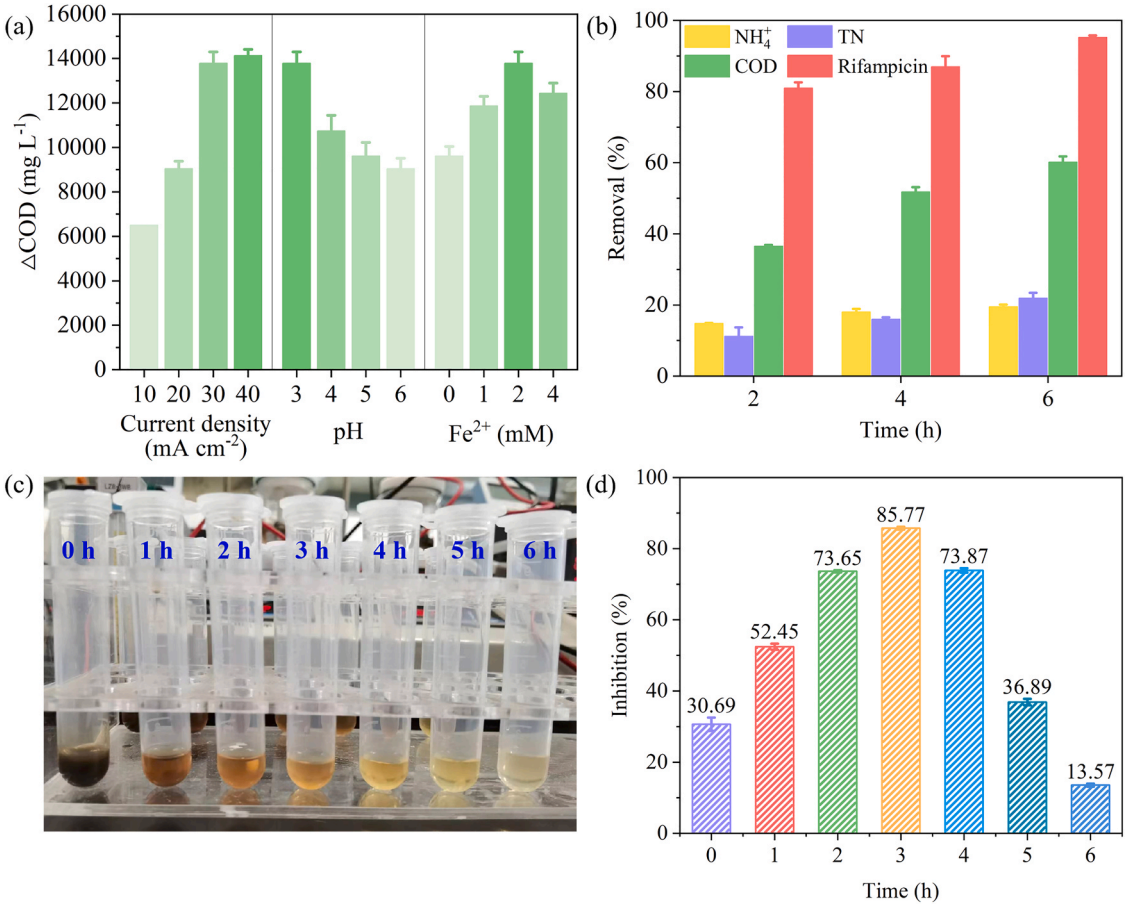

Fig. 5. (a) Effect of current density, initial pH and Fe^{2+} dosage on COD removal at 6 h. (b) The NH_4^+, TN, COD and rifampicin removal under optimal conditions (current density = 30 mA cm^{-2}, pH 3 and 2 mM Fe^{2+}). (c) Pictures of samples collected at different treatment times. (d) Inhibition of the luminescence of *Vibrio fischeri* bacteria after 15 min exposure.

vertices, ensuring continuous electron transfer for ORR. Exposing the electrode to air allowed self-breathing and oxygen transfer through the hydrophobic microenvironments of the electrode, achieving the effective oxygen diffusion coefficient of 2.56 × 10^{-6} m^2 s^{-1}. Integration of PESA into the electrolyte performed dual roles: stabilization of H_2O_2 through H-boding and inhibition of scale formation on the electrode. When constructing the self-breathing electro-Fenton system to treat industrial pharmaceutical wastewater, a COD removal rate of 60.21 ± 1.58% and was achieved and the rifampicin removal rate was as high as 95.29 ± 1.58% after 6 hours of electrolysis. The findings underscore the pivotal role in enhancing the efficiency and sustainability of industrial wastewater treatment processes.

CRediT authorship contribution statement

Yingshi Zhu: Writing – original draft, Visualization, Software, Methodology, Investigation, Funding acquisition, Formal analysis, Data curation, Conceptualization. **Jianqiu Zhu:** Writing – review & editing, Supervision, Resources, Project administration. **Huabin ShenTu:** Writing – review & editing, Supervision, Project administration. **Genman Lin:** Writing – review & editing, Supervision, Project administration. **Jun Wei:** Writing – review & editing, Supervision. **Yanfei Wei:** Writing – review & editing, Supervision, Project administration. **Lecheng Lei:** Writing – review & editing, Supervision, Project administration. **Yuru Li:** Writing – review & editing, Supervision. **Tao Yu:** Writing – review & editing, Supervision. **Zhongjian Li:** Writing – review & editing, Supervision. **Yang Hou:** Writing – review & editing, Supervision. **Bin Yang:** Writing – review & editing, Validation, Supervision, Resources, Project, administration, Funding acquisition.

Declaration of Competing Interest

The authors declare that they have no known competing financial interests or personal relationships that could have appeared to influence the work reported in this paper.

Data availability

Data will be made available on request.

Acknowledgements

This work was financially supported by the “Lingyan” R&D Plan Project of Zhejiang Province (2023C03140), the China Postdoctoral Science Foundation (2023M733062), the National Natural Science Foundation of China (22278366, 22238008 and 21878271) and the Project of Zhejiang Society for Environmental Sciences (2023HT0037).

Appendix A. Supporting information

Supplementary data associated with this article can be found in the online version at doi:10.1016/j.apcatb.2024.123973.

References

[1] M. Lee, T. Merle, D. Rentsch, S. Canonica, U. von Gunten, Abatement of polychloro-1,3-butadienes in aqueous solution by ozone, UV photolysis, and advanced

oxidation processes (O_3/H_2O_2 and UV/H_2O_2), Environ. Sci. Technol. 51 (2017) 497–505, https://doi.org/10.1021/acs.est.6b04506.
[2] S. Liu, D. Liu, Y. Sun, P. Xiao, H. Lin, J. Chen, X. Wu, X. Duan, S. Wang, Enzyme-mimicking single-atom FeN_4 sites for enhanced photo-Fenton-like reactions, Appl. Catal. B. 310 (2022) 121327, https://doi.org/10.1016/j.apcatb.2022.121327.
[3] G. Wang, K. Tang, A.C. Hambly, Y. Zhang, H.R. Andersen, Sustainable and reagentless Fenton treatment of complex wastewater, Environ. Sci. Technol. 57 (2023) 626–634, https://doi.org/10.1021/acs.est.2c06702.
[4] D. Zhong, Z. Zhou, W. Ma, J. Ma, W. Lv, W. Feng, X. Du, F. He, Study on degradation of chloramphenicol by H_2O_2/PMS double-oxidation system catalyzed by pipe deposits from water networks, J. Environ. Chem. Eng. 10 (2022) 107529, https://doi.org/10.1016/j.jece.2022.107529.
[5] J. Chang, Q. Li, J. Shi, M. Zhang, L. Zhang, S. Li, Y. Chen, S. Li, Y. Lan, Oxidation-reduction molecular junction covalent organic frameworks for full reaction photosynthesis of H_2O_2, Angew. Chem. Int. Ed. 62 (2023) e202218868, https://doi.org/10.1002/anie.202218868.
[6] J. An, N. Li, Y. Wu, S. Wang, C. Liao, Q. Zhao, L. Zhou, T. Li, X. Wang, Y. Feng, Revealing decay mechanisms of H_2O_2-based electrochemical advanced oxidation processes after long-term operation for phenol degradation, Environ. Sci. Technol. 54 (2020) 10916–10925, https://doi.org/10.1021/acs.est.0c03233.
[7] Y. Peng, Z. Bian, W. Zhang, H. Wang, Identifying the key N species for electrocatalytic oxygen reduction reaction on N-doped graphene, Nano Res 16 (2023) 6642–6651, https://doi.org/10.1007/s12274-023-5421-0.
[8] J. An, Y. Feng, Q. Zhao, X. Wang, J. Liu, N. Li, Electrosynthesis of H_2O_2 through a two-electron oxygen reduction reaction by carbon based catalysts: From mechanism, catalyst design to electrode fabrication, Environ. Sci. Ecotechnol. 11 (2022) 100170, https://doi.org/10.1016/j.ese.2022.100170.
[9] Y. Gao, W. Zhu, Y. Li, Q. Zhang, H. Chen, J. Zhang, T. Huang, Anthraquinone (AQS)/polyaniline (PANI) modified carbon felt (CF) cathode for selective H_2O_2 generation and efficient pollutant removal in electro-Fenton, J. Environ. Manag. 304 (2022) 114315, https://doi.org/10.1016/j.jenvman.2021.114315.
[10] M. Muñoz-Morales, A. Ramírez, A. Cañizares, J. Llanos, C. Ania, Evaluating key properties of carbon materials as cathodes for the electrogeneration of hydrogen peroxide, Carbon 210 (2023) 118082, https://doi.org/10.1016/j.carbon.2023.118082.
[11] M. Hou, S. Gong, L. Ji, J. Huang, M. Xu, Z. Chen, Three-dimensional porous ultrathin carbon networks reinforced PBAs-derived electrocatalysts for efficient oxygen evolution, Chem. Eng. J. 419 (2021) 129575, https://doi.org/10.1016/j.cej.2021.129575.
[12] M. Tian, J. Wu, R. Li, Y. Chen, D. Long, Fabricating a high-energy-density supercapacitor with asymmetric aqueous redox additive electrolytes and free-standing activated-carbon-felt electrodes, Chem. Eng. J. 363 (2019) 183–191, https://doi.org/10.1016/j.cej.2019.01.070.
[13] J. Quílez-Bermejo, E. Morallón, D. Cazorla-Amorós, Metal-free heteroatom-doped carbon-based catalysts for ORR: a critical assessment about the role of heteroatoms, Carbon 165 (2020) 434–454, https://doi.org/10.1016/j.carbon.2020.04.068.
[14] L. Xie, W. Zhou, Z. Qu, Y. Ding, J. Gao, F. Sun, Y. Qin, Understanding the activity origin of oxygen-doped carbon materials in catalyzing the two-electron oxygen reduction reaction towards hydrogen peroxide generation, J. Colloid Interface Sci. 610 (2022) 934–943, https://doi.org/10.1016/j.jcis.2021.11.144.
[15] H. Zhang, Y. Li, H. Zhang, G. Li, F. Zhang, A three-dimensional floating air cathode with dual oxygen supplies for energy-efficient production of hydrogen peroxide, Sci. Rep. 9 (2019) 1817, https://doi.org/10.1038/s41598-018-37919-3.
[16] S. Guo, M. Chen, Q. Zeng, J.E. Yang, J. Xie, Y. Wang, Q. Sun, Energy-efficient H_2O_2 electro-production based on an integrated natural air-diffusion cathode and its application, ACS EST Water 2 (2022) 1647–1658, https://doi.org/10.1021/acsestwater.2c00160.
[17] J. Xie, J. Jing, J. Gu, J. Guo, Y. Li, M. Zhou, Hydrogen peroxide generation from gas diffusion electrode for electrochemical degradation of organic pollutants in water: a review, J. Environ. Chem. Eng. 10 (2022) 107882, https://doi.org/10.1016/j.jece.2022.107882.
[18] C. Yang, F. Sun, Z. Qu, X. Li, W. Zhou, J. Gao, Interfacial O_2 accumulation affects microenvironment in carbon-based electrocatalysts for H_2O_2 production, ACS Energy Lett. 7 (2022) 4398–4407, https://doi.org/10.1021/acsenergylett.2c02021.
[19] F. Yu, Y. Chen, Y. Pan, Y. Yang, H. Ma, A cost-effective production of hydrogen peroxide via improved mass transfer of oxygen for electro-Fenton process using the vertical flow reactor, Sep. Purif. Technol. 241 (2020) 116695, https://doi.org/10.1016/j.seppur.2020.116695.
[20] Q. Zhang, M. Zhou, G. Ren, Y. Li, Y. Li, X. Du, Highly efficient electrosynthesis of hydrogen peroxide on a superhydrophobic three-phase interface by natural air diffusion, Nat. Commun. 11 (1) (2020) 11, https://doi.org/10.1038/s41467-020-15597-y.
[21] A. Spector, W. Ma, R.R. Wang, The aqueous humor is capable of generating and degrading H_2O_2, Invest. Ophthalmol. Vis. Sci. 39 (1998) 1188.
[22] J. Liu, C. Lv, Synthesizing environmentally friendly non-silicone oxygen bleaching stabilizer for linen yarn using oligomeric acrylic acid, Sci. Rep. 11 (2021) 10355, https://doi.org/10.1038/s41598-021-89888-9.
[23] Y. Ma, E. Zhao, G. Xia, J. Zhan, G. Yu, Y. Wang, Effects of water constituents on the stability of gas diffusion electrode during electrochemical hydrogen peroxide production for water and wastewater treatment, Water Res. 229 (2023) 119503, https://doi.org/10.1016/j.watres.2022.119503.
[24] C. Cui, S. Zhang, Synthesis, characterization and performance evaluation of an environmentally benign scale inhibitor IA/AMPS co-polymer, New. J. Chem. 43 (2019) 9472–9482, https://doi.org/10.1039/c9nj01355e.
[25] Y. Zheng, J. He, S. Qiu, D. Yu, Y. Zhu, H. Pang, J. Zhang, Boosting hydrogen peroxide accumulation by a novel air-breathing gas diffusion electrode in electro-Fenton system, Appl. Catal. B. 316 (2022) 121617, https://doi.org/10.1016/j.apcatb.2022.121617.
[26] Y. Cao, S. Zhang, B. Zhang, C. Han, Y. Zhang, X. Wang, S. Liu, H. Gong, X. Liu, S. Fang, F. Pan, J. Sun, Local electric field promoted kinetics and interfacial stability of a phosphorus anode with ionic covalent organic frameworks, Adv. Mater. 35 (2023) e2208514, https://doi.org/10.1002/adma.202208514.
[27] J. An, N. Li, Q. Zhao, Y. Qiao, S. Wang, C. Liao, L. Zhou, T. Li, X. Wang, Y. Feng, Highly efficient electro-generation of H_2O_2 by adjusting liquid-gas-solid three phase interfaces of porous carbonaceous cathode during oxygen reduction reaction, Water Res. 164 (2019) 114933, https://doi.org/10.1016/j.watres.2019.114933.
[28] P. Cordeiro-Junior, B.J. Lobato, M. Lanza, R.M. Rodrigo, Highly efficient electrochemical production of hydrogen peroxide using the GDE technology, Ind. Eng. Chem. Res. 61 (2022) 10660–10669, https://doi.org/10.1021/acs.iecr.2c01669.
[29] H.C.L. Geraldino, T.K.F.S. Freitas, D.D. Manholer, F. França, J.H. Oliveira, E. A. Volnistem, A.R.F. Lima, M. Bertotti, E.M. Girotto, J.C. Garcia, Electrochemical generation of H_2O_2 using gas diffusion electrode improved with rGO intensified with the Fe_3O_4/GO catalyst for degradation of textile wastewater, J. Water Process. Eng. 36 (2020) 101377, https://doi.org/10.1016/j.jwpe.2020.101377.
[30] M. Li, X. Qin, M. Gao, T. Li, Y. Lv, Graphitic carbon nitride and carbon nanotubes modified active carbon fiber cathode with enhanced H_2O_2 production and recycle of Fe^{3+}/Fe^{2+} for electro-Fenton treatment of landfill leachate concentrate, Environ. Sci. Nano 9 (2022) 632–652, https://doi.org/10.1039/D1EN01095F.
[31] J. Lu, X. Liu, Q. Chen, J. Zhou, Coupling effect of nitrogen-doped carbon black and carbon nanotube in assembly gas diffusion electrode for H_2O_2 electro-generation and recalcitrant pollutant degradation, Sep. Purif. Technol. 265 (2021) 118493, https://doi.org/10.1016/j.seppur.2021.118493.
[32] J. Moreira, V. Bocalon Lima, L. Athie Goulart, M.R.V. Lanza, Electrosynthesis of hydrogen peroxide using modified gas diffusion electrodes (MGDE) for environmental applications: quinones and azo compounds employed as redox modifiers, Appl. Catal. B. 248 (2019) 95–107, https://doi.org/10.1016/j.apcatb.2019.01.071.
[33] T.O. Silva, L.A. Goulart, I. Sánchez-Montes, G.O.S. Santos, R.B. Santos, R. Colombo, M.R.V. Lanza, Using a novel gas diffusion electrode based on PL6 carbon modified with benzophenone for efficient H_2O_2 electrogeneration and degradation of ciprofloxacin, Chem. Eng. J. 455 (2023) 140697, https://doi.org/10.1016/j.cej.2022.140697.
[34] S. Wang, D. Ye, X. Zhu, Y. Yang, J. Chen, Z. Liu, R. Chen, Q. Liao, Beyond the catalyst: a robust and omnidirectional hydrophobic triple-phase architecture for ameliorating air-breathing H_2O_2 electrosynthesis and wastewater remediation, Sep. Purif. Technol. 305 (2023) 122397, https://doi.org/10.1016/j.seppur.2022.122397.
[35] P. Wu, Y. Zhang, Z. Chen, Y. Duan, Y. Lai, Q. Fang, F. Wang, S. Li, Performance of boron-doped graphene aerogel modified gas diffusion electrode for in-situ metal-free electrochemical advanced oxidation of Bisphenol A, Appl. Catal. B. 255 (2019) 117784, https://doi.org/10.1016/j.apcatb.2019.117784.
[36] Y. Konno, T. Yamamoto, T. Nagayama, Nanoporous manganese ferrite films by anodising electroplated Fe-Mn alloys for bifunctional oxygen electrodes, Nanoscale 13 (2021) 12738–12749, https://doi.org/10.1039/d1nr02457d.
[37] W. Zhou, L. Xie, J. Gao, R. Nazari, H. Zhao, X. Meng, F. Sun, G. Zhao, J. Ma, Selective H_2O_2 electrosynthesis by O-doped and transition-metal-O-doped carbon cathodes via O_2 electroreduction: a critical review, Chem. Eng. J. 410 (2021) 128368, https://doi.org/10.1016/j.cej.2020.128368.
[38] H. Gong, S. Kim, J.D. Lee, S. Yim, Simple quantification of surface carboxylic acids on chemically oxidized multi-walled carbon nanotubes, Appl. Surf. Sci. 266 (2013) 219–224, https://doi.org/10.1016/j.apsusc.2012.11.152.
[39] X. Lu, D. Wang, K. Wu, X. Guo, W. Qi, Oxygen reduction to hydrogen peroxide on oxidized nanocarbon: identification and quantification of active sites, J. Colloid Interface Sci. 573 (2020) 376–383, https://doi.org/10.1016/j.jcis.2020.04.030.
[40] S. Chen, T. Luo, K. Chen, Y. Lin, J. Fu, K. Liu, C. Cai, Q. Wang, H. Li, X. Li, J. Hu, H. Li, M. Zhu, M. Liu, Chemical identification of catalytically active sites on oxygen-doped carbon nanosheet to decipher the high activity for electro-synthesis hydrogen peroxide, Angew. Chem. Int. Ed. 60 (2021) 16607–16614, https://doi.org/10.1002/anie.202104480.
[41] A.K.C. Wong, R. Banerjee, A. Bazylak, Tuning MPL intrusion to increase oxygen transport in dry and partially saturated polymer electrolyte membrane fuel cell gas diffusion layers, J. Electrochem. Soc. 166 (2019) F3009–F3019, https://doi.org/10.1149/2.0021907jes.
[42] Z. Song, C. Xu, X. Sheng, X. Feng, L. Jiang, Utilization of peroxide reduction reaction at air-liquid-solid joint interfaces for reliable sensing system construction, Adv. Mater. 30 (2018) 1701473, https://doi.org/10.1002/adma.201701473.
[43] T. Lu, Q. Chen, Independent gradient model based on Hirshfeld partition: a new method for visual study of interactions in chemical systems, J. Comput. Chem. 43 (2022) 539–555, https://doi.org/10.1002/jcc.26812.
[44] F. Deng, H. Olvera-Vargas, M. Zhou, S. Qiu, I. Sires, E. Brillas, Critical review on the mechanisms of Fe^{2+} regeneration in the electro-Fenton process: fundamentals and boosting strategies, Chem. Rev. 123 (2023) 4635–4662, https://doi.org/10.1021/acs.chemrev.2c00684.
[45] J.L.D.S. Duarte, A.M.S. Solano, M.L.P.M. Arguelho, J. Tonholo, C.A. Martínez-Huitle, C.L.D.P. Zanta, Evaluation of treatment of effluents contaminated with rifampicin by Fenton, electrochemical and associated processes, J. Water Process. Eng. 22 (2018) 250–257, https://doi.org/10.1016/j.jwpe.2018.02.012.

[46] E. Brillas, Fenton, photo-Fenton, electro-Fenton, and their combined treatments for the removal of insecticides from waters and soils. A review, Sep. Purif. Technol. 284 (2022) 120290, https://doi.org/10.1016/j.seppur.2021.120290.
[47] J. Liao, S. Xie, J. Yao, D. Xu, P. Liao, Efficient hydrogen peroxide production at high current density by air diffusion cathode based on pristine carbon black, J. Electroanal. Chem. 904 (2022) 115938, https://doi.org/10.1016/j.jelechem.2021.115938.
[48] M. Liu, Z. Feng, X. Luan, W. Chu, H. Zhao, G. Zhao, Accelerated Fe^{2+} regeneration in an effective electro-Fenton process by boosting internal electron transfer to a nitrogen-conjugated Fe(III) complex, Environ. Sci. Technol. 55 (2021) 6042–6051, https://doi.org/10.1021/acs.est.0c08018.
[49] Y. Zhu, J. Zhu, H. ShenTu, Y. Wei, J. Wei, L. Lei, Y. Li, T. Yu, Z. Li, Y. Hou, B. Yang, Deformation of charge density activated by conductive carbon with the piezoelectric effect of tourmaline for highly promoting Fe^{3+}/Fe^{2+} cycle in Fenton-like process, Appl. Catal. B. 334 (2023) 122824, https://doi.org/10.1016/j.apcatb.2023.122824.
[50] Z. He, J. Chen, Y. Chen, C.P. Makwarimba, X. Huang, S. Zhang, J. Chen, S. Song, An activated carbon fiber-supported graphite carbon nitride for effective electro-Fenton process, Electrochim. Acta 276 (2018) 377–388, https://doi.org/10.1016/j.electacta.2018.04.195.
[51] Z. Liu, S. Dong, D. Zou, J. Ding, A. Yu, J. Zhang, C. Shan, G. Gao, B. Pan, Electrochemically mediated nitrate reduction on nanoconfined zerovalent iron: Properties and mechanism, Water Res 173 (2020) 115596, https://doi.org/10.1016/j.watres.2020.115596.
[52] Y. Zhu, S. Qiu, F. Deng, Y. Zheng, K. Li, F. Ma, D. Liang, Enhanced degradation of sulfathiazole by electro-Fenton process using a novel carbon nitride modified electrode, Carbon 145 (2019) 321–332, https://doi.org/10.1016/j.carbon.2019.01.032.
[53] L. He, Y. Ji, J. Cheng, C. Wang, L. Jiang, X. Chen, H. Li, S. Ke, J. Wang, Effect of pH and Cl^- concentration on the electrochemical oxidation of pyridine in low-salinity reverse osmosis concentrate: kinetics, mechanism, and toxicity assessment, Chem. Eng. J. 449 (2022) 137669, https://doi.org/10.1016/j.cej.2022.137669.